*Technical Article*

# State of the Art in the Simulation of Electromagnetic Fields based on Large Scale Finite Element Eigenanalysis

***Abstract* — In particle accelerator physics, charged particles are accelerated within highly resonating structures with the help of high frequency electromagnetic fields. The precise knowledge of the field distribution in the devices is of paramount importance for accurate beam dynamics simulations. Because of the request to consider even small field deviations attributed to fine three-dimensional geometry details, the necessary accurate numerical modeling results in a demanding computation task. This challenging problem can be addressed on the basis of accurate curvilinear finite elements which are able to capture the non-flat shape of typically applied superconducting resonator structures in combination with a fine computational mesh. The resulting large electromagnetic models are simulated on a distributed memory architecture using the MPI parallelization strategy.**

## I. Introduction

In particle accelerator physics, the determination of the radio frequency electromagnetic fields excited on purpose in highly resonating cavities is preferably performed in the frequency domain using an appropriate eigenmode analysis [1]-[3]. The corresponding continuous vector valued equations can be solved exactly only for a limited number of problems with reasonable complexity. Problems of practical importance can only be solved approximately on a discretized level.

A popular discretization scheme is given with the finite element method (FEM) in the frequency domain employing a plain tetrahedral mesh which enables an approximation of the field distribution with high accuracy [4]-[6]. The ever increasing demand for high precision modeling can further be supported by introducing a higher order geometry approximation in case curved material interfaces have to be considered. The usage of the curvilinear finite elements is particular advantageous when local planar approximations are not accurate enough to handle sensitive material interfaces or boundary conditions [7]-[18]. The precise modeling of realistic electromagnetic problems is naturally accompanied by the necessity to employ huge memory resources and requires long simulation times. Extremely high computational resources prohibit the usage of classical implementations while a proper parallelization strategy on a distributed memory architecture enables a reliable execution and simultaneously keeps the solution times on an acceptable level [20]-[23].

To address carefully the challenging issues mentioned above, the article is organized as follows: in Section II, a short review of the fundamental continuous equations is given and the description on the calculation of the FEM stiffness and mass matrices for the numerical evaluation using curvilinear geometry transformation is presented in Section III. Programming details are highlighted in Section IV and a convergence analysis applied to verify a proper implementation of the underlying algorithms is given in Section V. Finally, in Section VI, the described algorithm is used to perform high precision eigenvalue calculations for the three-dimensional (3D) TESLA 'Third Harmonic' (3rd) structure.

## II. Fundamental Continuous Equations

The fundamental properties of the applied high frequency electromagnetic fields are described by the Maxwell's equations. In the context of highly resonating structures, they are preferably formulated in the frequency domain following the notation

$$\begin{aligned} \operatorname{curl} \vec{\mathrm{H}}(\vec{r}) &= \vec{\mathrm{J}}(\vec{r}) + \mathrm{j}\omega\vec{D}(\vec{r}) \\ \operatorname{curl} \vec{E}(\vec{r}) &= -j\omega\vec{B}(\vec{r}) \\ \operatorname{div} \vec{D}(\vec{r}) &= \rho(\vec{r}) \\ \operatorname{div} \vec{B}(\vec{r}) &= 0 \end{aligned} \tag{1}$$

with the magnetic and electric field strengths $\vec{H}$ and $\vec{E}$, the magnetic and electric flux densities $\vec{B}$ and $\vec{D}$ and the angular frequency $\omega = 2\pi f$. The sources are specified by the electric current density $\vec{J}$ and the electric charge density $\rho$. Assuming isotropic material distributions inside the resonators, the underlying material relations are stated as

$$\begin{aligned} \vec{D}(\vec{r}) &= \varepsilon(\vec{r})\,\vec{E}(\vec{r}) \\ \vec{B}(\vec{r}) &= \mu(\vec{r})\,\vec{H}(\vec{r}) \end{aligned} \tag{2}$$

employing the scalar permittivity $\varepsilon$ and the scalar permeability $\mu$. In the absence of any sources, the problem can naturally be reduced to an eigenvalue formulation. The fundamental equation is obtained by inserting the material relations (2) into the set of Maxwell's equations (1) and stating the description for the electric field strength while eliminating the magnetic field strength. Combining the two curl equations into a single double curl variant results in

$$\operatorname{curl}\frac{1}{\mu(\vec{r})}\operatorname{curl}\vec{E}(\vec{r}) = \omega^2\varepsilon(\vec{r})\,\vec{E}(\vec{r}) \tag{3}$$

which can be further modified using relative material parameters according to $\varepsilon = \varepsilon_{\mathrm{r}}\varepsilon_0$ and $\mu = \mu_{\mathrm{r}}\mu_0$ with the free space material parameters $\varepsilon_0$ and $\mu_0$. Additionally, the speed of light in free space, $c_0 = 1/\sqrt{\mu_0\varepsilon_0}$, is used to normalize the eigenvalue. According to the Maxwell's equations, the resulting continuous eigenvalue formulation

$$\operatorname{curl}\frac{1}{\mu_{\mathrm{r}}(\vec{\mathrm{r}})}\operatorname{curl}\vec{E}(\vec{\mathrm{r}}) = \left(\frac{\omega}{c_0}\right)^2 \varepsilon_{\mathrm{r}}(\vec{\mathrm{r}})\,\vec{E}(\vec{\mathrm{r}})\Big|_{\vec{r}\in\Omega} \tag{4}$$

has to be accompanied by the indispensable divergence constraint

$$\operatorname{div}\left(\varepsilon_{\mathrm{r}}(\vec{\mathrm{r}})\,\varepsilon_0\vec{E}(\vec{\mathrm{r}})\right)=0\Big|_{\vec{r}\in\Omega} \tag{5}$$

which also has to be hold for all points $\vec{r}$ within the computational domain $\Omega$. In the presence of superconducting cavities, the perfect electric conducting boundary condition

$$\vec{n}\times\vec{E}(\vec{\mathrm{r}})=0\Big|_{\vec{r}\in\partial\Omega} \tag{6}$$

can readily be applied for all points on the boundary $\partial\Omega$, where the symbol $\vec{n}$ represents a vector normal to the surface at the specified position $\vec{r}$. In particular, if dedicated structural elements are introduced into the device to excite on purpose the electromagnetic fields, the simplified condition (6) has to be replaced accordingly at least on those parts of the surface which will identify the port regions.

## III. Finite Element Method

During the last decades, various discretization techniques have been developed with individual advantages depending on the aspired applications. In the current work, the focus is put on the classical finite element method with vector valued basis functions on tetrahedral elements in a hierarchical setup [7]-[13]. A proper approximation of the continuous distribution of the electric field strength specified in (4) is given by the local Ritz approach according to

$$\vec{E}(\vec{r})=\sum_{i=1}^{n}c_i\,\vec{w}_i(\vec{r}) \tag{7}$$

with scalar weighting coefficients $c_i$ and vector valued basis functions $\vec{w}_i$ with local support. Insertion of the approximation (7) into the continuous eigenvalue formulation (4) and application of a Galerkin test for the resulting expression leads to the discrete eigenvalue formulation

$$A\,\vec{c}=\lambda\,B\,\vec{c} \tag{8}$$

where $A=(A_{ij}),\ i,j=1,\ldots,n$ is known as the FEM stiffness matrix and $B=(B_{ij}),\ i,j=1,\ldots,n$ as the FEM mass matrix. The parameter $\lambda=(\omega/c_0)^2$ represents the eigenvalue corresponding to the eigenvector $\vec{c}=(c_i)$. The obtained matrix coefficients

$$\begin{aligned}A_{ij}&=\iiint_{\Omega}\operatorname{curl}\left(\frac{1}{\mu_r}\operatorname{curl}\vec{w}_i\right)\cdot\vec{w}_j\,\mathrm{d}\Omega\\ B_{ij}&=\iiint_{\Omega}\varepsilon_r\,\vec{w}_i\cdot\vec{w}_j\,\mathrm{d}\Omega\end{aligned} \tag{9}$$

are further modified with the help of integration by parts and applying Gauß-Ostrogradski's theorem.

This procedure results in an additional surface integral term

$$\sum_{i=1}^{n}c_i\iint_{\Gamma=\partial\Omega}\left(\frac{1}{\mu_r}\operatorname{curl}\vec{w}_i\right)\times\vec{w}_j\cdot\vec{n}\,\mathrm{d}\Gamma \tag{10}$$

which vanishes if only perfect magnetic or perfect electric boundary conditions are applied.

In the first case, the scalar triple product evaluates to zero because the magnetic flux density is parallel to the normal vector per definition whereas in the latter case only test functions $\vec{w}_j$ with normal components on the surface have to be considered. Following the specified conditions, the matrix elements

$$\begin{aligned}A_{ij}&=\iiint_{\Omega}\frac{1}{\mu_r}\operatorname{curl}\vec{w}_i\cdot\operatorname{curl}\vec{w}_j\,\mathrm{d}\Omega\\ B_{ij}&=\iiint_{\Omega}\varepsilon_r\,\vec{w}_i\cdot\vec{w}_j\,\mathrm{d}\Omega\end{aligned} \tag{11}$$

have to be evaluated within the computational domain $\Omega$. Due to the compact support of the applied basis functions, the populations of the matrices A and B are very sparse. The integration in (11) has to be performed for each element independent of the neighbors and is followed by a subsequent summation of the individual contributions. This naturally allows assembling the entire sparse matrix in an efficient parallel strategy. Each individual contribution from an element indicated by superscript *e* can be summarized to

$$\begin{aligned}A_{ij}^{\mathrm{e}}&=\frac{1}{\mu_r^e}\iiint_{\Omega_0}\operatorname{curl}\vec{w}_i\cdot\operatorname{curl}\vec{w}_j\,|J|\,\mathrm{d}\Omega\\ B_{ij}^{\mathrm{e}}&=\varepsilon_r^e\iiint_{\Omega_0}\vec{w}_i\cdot\vec{w}_j\,|J|\,\mathrm{d}\Omega.\end{aligned} \tag{12}$$

where the material distribution is approximated for simplicity reasons with constant values for each element. The integration in (12) is accomplished on a unit tetrahedron $\Omega_0$. The symbol $J$ denotes the Jacobian matrix of the applied geometrical transformations and $|J|$ is used to identify its determinant.

In the simplest approach, the geometry transformation follows the form

$$\vec{r}(\vec{u})=\sum_{i=1}^{p}\vec{r}_i\,\varphi_i(\vec{u}) \tag{13}$$

utilizing the control parameters $\vec{r}_i$ together with the scalar basis functions $\varphi_i(\vec{u})$ which span the FEM scalar spaces. Following the notations $\vec{r}=(r_1,r_2,r_3)$ and $\vec{u}=(u_1,u_2,u_3)$ the Jacobian can be easily evaluated according to the definition

$$J=(J_{ij})=\left(\frac{\partial r_j}{\partial u_i}\right). \tag{14}$$

In case of the widespread linear transformation, the Jacobian is constant which simplifies the integration process in (12). In order to improve the accuracy of the spatial approximation in those cases where non-flat material interfaces are involved, the linear mapping of a unit tetrahedron to any element of the mesh is replaced by a nonlinear variant.

For this purpose, according to the transformation (13), the set of lowest order scalar basis functions is extended by higher order polynomials. On the one hand, increasing the desired order for the interpolation leads to the more geometrically flexible transformation; on the other hand, it simultaneously

increases the numerical effort since more control points have to be involved in the calculation process.

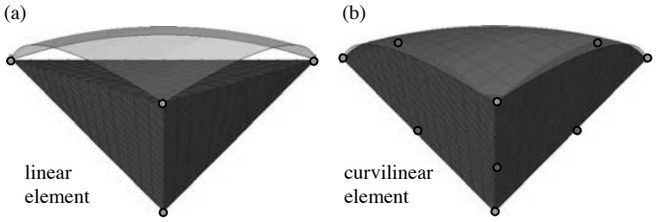


Fig. 1. Linear versus curvilinear (here: quadratic polynomial) transformation of a unit tetrahedron conforming to a sphere of radius 2 touching the element in tree corner points.

Quadratic polynomial interpolation as the simplest nonlinear representative requires the knowledge of ten control points per tetrahedron, where four of them are typically allocated on the corners of the element and the remaining six are usually placed in the center of the corresponding edges. Thus, each face is represented by a function of second order behavior and can smoothly fit to curvilinear interfaces. In case of hierarchical scalar basis functions, the control vectors are represented by difference vectors from the edge centers to the surface points instead of the surface vectors itself. In Fig. 1, the two specified approaches are visualized. The vector valued basis functions $\vec{w}_i$ and their rotations $\operatorname{curl} \vec{w}_i$ can be expressed within a certain element by the fixed local basis functions $\vec{w}_i'$ defined on a unit tetrahedron [7]-[13] via the transformations

$$\vec{w}_i = (J^{-1})^{\mathrm{T}}\, \vec{w}_i' \quad \text{and} \quad \operatorname{curl} \vec{w}_i = \frac{1}{|J|} J\, \operatorname{curl} \vec{w}_i' . \quad (15)$$

The calculations of the element matrices contributions according to (12) and (15) can be carried out analytically for linear geometry transformations. The resulting simple expressions enable then fast and accurate assembly of the whole system matrices. In case of higher order spatial transformations with curvilinear elements, the exact evaluation is expensive and a numerical integration technique with sufficient accuracy is employed instead. As soon as the element matrices are calculated, the assembly of the entire system of equations can be performed by means of inserting the local values into the global system.

## IV. Implementation

The geometric modeling of the structure is performed within the CST Studio Suite® which is also used for the tetrahedral meshing [19]. The necessary information is passed to the FEM program by means of ASCII or binary file transfer. The entire FEM algorithm is implemented in C++ thus enabling high performance evaluation and a clear code layout [20]. The external mesh information is used in a first step to set up a graph representing the population pattern of the sparse stiffness and mass matrices in a way that only the degrees of freedom (DoFs) are considered. Constraints placed due to boundary conditions are incorporated in the matrix setup.

Firstly, the entire graph is arbitrarily distributed among all the contributing processes but it has to be partitioned in proper clusters of contiguous elements to keep the communication overhead during the computations low. An example is displayed in Fig.2, where the formation of the desired domains with the help of the segmentation process can be seen.

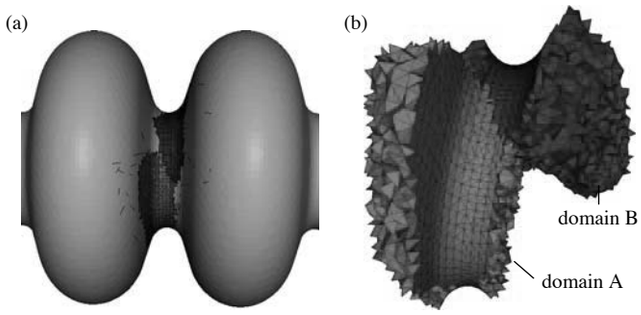


Fig. 2. Distribution of the computational grid among various processes. Two selected regions are shown in (a) for the iris region of a resonator model. The DoFs located in the interface plane between different regions (b) have to be assigned properly in order to keep the communication overhead small.

The final distribution of the various DoFs among the processes is determined with the help of the graph partitioning library ParMeTiS [21]. The knowledge of an advantageous numbering for the various DoFs is essential for the allocation of the required memory and setting up the matrices in the preferred communication-optimized way. Once the mesh and material information are properly distributed among all the processes, an efficient assembly of the global matrices according to the procedure described in Section III can be performed. A suitable handling of the matrices can be achieved by means of the software package PETSc [22], which provides different linear solvers and various preconditioners.

Instead of direct distribution of the DoFs among the various processes and the following selection of the appropriate local mesh cells afterwards, it is more convenient for the graph partitioner to distribute the mesh cells first and to split then the DoFs using for example a heuristic approach for values located within the interface planes. This is true at least for the higher order approximation schemes where the number of elements is much smaller compared to the number of DoFs, and the underlying graph is considerably smaller and is therefore easier to split up.

In this sense, one can even further simplify the partitioning process and set up a graph representing the distribution of only the grid nodes which further reduces the graph size. In a subsequent step, one has to find a local distribution of elements and DoFs such that these quantities are equally distributed among the various processes as good as possible. In Table I, two different variants enabling the decomposition procedure are evaluated and compared to each other taking into account a representative mesh of a practical application.

Following the data specified in Table I and II, one can clearly see that the subdivision of a given volume into multiple non-overlapping parts consistently increases the communication expenses because less information is available in the local matrices. This general law is based on geometric reasons due to the increasing overall surface and is therefore independent of the realized partitioning scheme. However, special care has to be taken to separate those values which are located in the interface plane between different regions. This is especially true for higher order approximation schemes where multiple DoFs are located on those boundary layers. As expected, the subdivision according to the DoFs leads to the most efficient partitioning. However, this achievement is accompanied by

high computational costs arising from the necessity to set up and split a huge connectivity graph. On the other hand, the simplest procedure to decompose the computational domain is to cluster the mesh nodes according to the element topology and to apply a heuristic approach to separate the DoFs. According to the data specified in Table I and II, this procedure also enables the decomposition in an acceptable manner. This simplified approach can be further refined in a second stage if it is combined with the DoFs separation technique when the input is limited to the results of the first stage.

TABLE I. PARTITIONING OF A MESH CONSISTING OF 1.904.470 TETRAHEDRA AMONG VARIOUS PROCESSES USING **LINEAR FIELD APPROXIMATION**. THE NUMBER OF NONZERO (NNZ) ENTRIES PER MATRIX IS DISTRIBUTED SUCH THAT MOST OF THE VALUES ARE STORED LOCALLY.

| processes | FEM 06, linear field approximation<br>2.137.087 DoFs, 34.095.837 nnz | |
|---|---|---|
| | scheme: nodes<br>4.607.450 branches | scheme: DoFs<br>31.958.750 branches |
| 2 | 2.466 cuts (0,054 %)<br>99,928 % local | 4.879 cuts (0,015 %)<br>99,971 % |
| 4 | 5.599 cuts (0,122 %)<br>99,824 % local | 17.571 cuts (0,055 %)<br>99,897 % local |
| 8 | 16.307 cuts (0,354 %)<br>99,477 % local | 57.624 cuts (0,180 %)<br>99,662 % local |
| 16 | 31.509 cuts (0,684 %)<br>99,002 % local | 136.820 cuts (0,428 %)<br>99,197 % local |
| 32 | 72.311 cuts (1,569 %)<br>97,692 % local | 278.485 cuts (0,871 %)<br>98,366 % local |
| 64 | 122.295 cuts (2,654 %)<br>96,045 % local | 482.078 cuts (1,508 %)<br>97,172 % local |

TABLE II. PARTITIONING OF A MESH CONSISTING OF 1.904.470 TETRAHEDRA AMONG VARIOUS PROCESSES USING **QUADRATIC FIELD APPROXIMATION**. THE NUMBER OF NONZERO (NNZ) ENTRIES PER MATRIX IS DISTRIBUTED SUCH THAT MOST OF THE VALUES ARE STORED LOCALLY.

| processes | FEM 20, quadratic field approximation<br>11.780.962 DoFs, 501.102.308 nnz | |
|---|---|---|
| | scheme: nodes<br>4.607.450 branches | scheme: DoFs<br>489.321.346 branches |
| 2 | 2.466 cuts (0,054 %)<br>99,923 % local | memory error |
| 4 | 5.599 cuts (0,122 %)<br>99,821 % local | memory error |
| 8 | 16.307 cuts (0,354 %)<br>99,466 % local | 650.286 cuts (0,133 %)<br>99,740 % local |
| 16 | 31.509 cuts (0,684 %)<br>98,976 % local | 1.587.394 cuts (0,324 %)<br>99,366 % local |
| 32 | 72.311 cuts (1,569 %)<br>97,627 % local | 3.228.226 cuts (0,660 %)<br>98,712 % local |
| 64 | 122.295 cuts (2,654 %)<br>95,943 % local | 5.646.508 cuts (1,154 %)<br>97,746 % local |

## V. CONVERGENCE ANALYSIS

In the following, we refer to the solution of Maxwell's equations within closed perfect conductive structures to verify the correctness of a proposed implementation of all involved algorithms. The usage of the mass and stiffness matrix description introduced in Section III allows setting up the discrete generalized eigenvalue problem (8) which is further solved numerically using our own implementation of the Jacobi-Davidson [24] algorithm. The knowledge of all components of the eigenvector $\vec{c}$ enables then to evaluate the expansion (7) of the electric field intensity in terms of the specified global basis functions. From the knowledge of the electric field strength distribution one can determine the magnetic flux density applying the curl operator. A convergence analysis is performed on the example of a spherical cavity embedded in a perfect electric conductive material where analytical solutions for all emerging modes can be derived. The degeneration of the examined modes in the symmetric resonator is not retained in a numerical study when the calculations are performed on an asymmetric tetrahedral grid. For a number of selected approximation schemes the obtained relative frequency error as a function of mesh cells utilizing an average over the degenerated modes is illustrated in Fig. 3 to Fig. 5. Additionally, the obtained convergence order based on this error definition is given for each scheme.

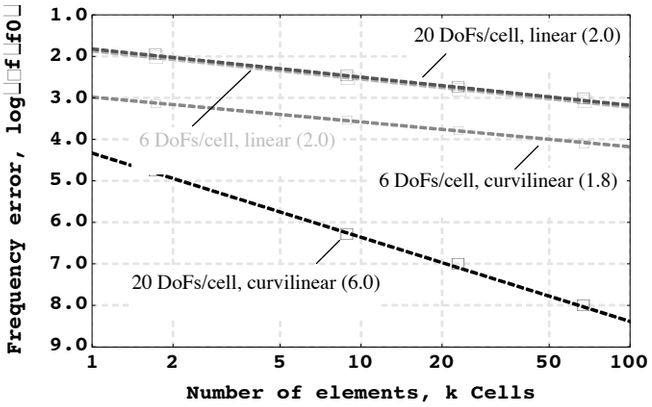


Fig. 3. Convergence analysis of various FEM approximations based on the resonance frequency of the fundamental mode (**TM 011**) in a spherical cavity with perfect electric conductive boundary conditions.

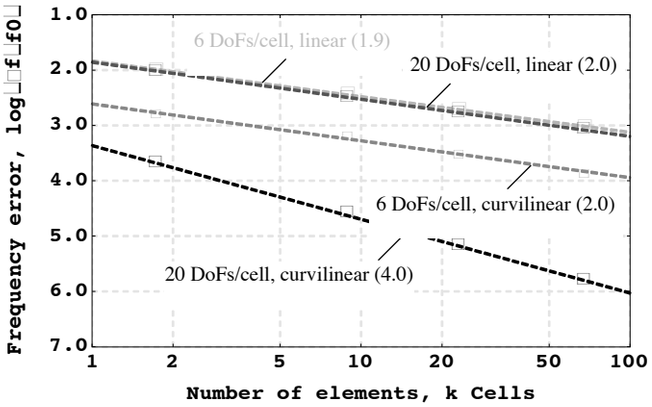


Fig. 4. Convergence analysis of various FEM approximations based on the resonance frequency of the first higher order modes (**TM 021, TM 121**) in a spherical cavity with perfect electric conductive boundary conditions.

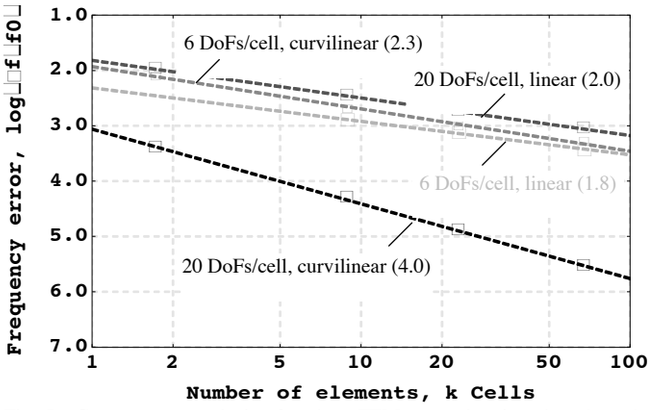


Fig. 5. Convergence analysis of various FEM approximations based on the resonance frequency of the second higher order mode (**TE 011**) in a spherical cavity with perfect electric conductive boundary conditions.

From these results one can clearly see that under linear geometry transformation, a second order field approximation (20 DoFs/cell) leads to nearly the same frequency deviation as the one obtained with the computationally cheaper first order scheme (6 DoFs/cell).

In contrast to what has been observed in [18], introducing a curvilinear geometry approximation even on the simple second order polynomial geometry transformation not only increases the overall accuracy here but additionally retains the higher order convergence of the quadratic field approximation scheme compared to the linear variant. We conclude that for the presented study all examined methods enabling linear geometric modeling suffer from an inexact boundary representation whereas the curvilinear geometric modeling overcomes this difficulty.

The presented convergence study is based on approximation functions of mixed order only. They are introduced to efficiently represent the field distribution in each computational element without the necessity of modeling all components. To extend the examination also to the complete field representations, a brick resonator of dimensions (2,e,π) is analyzed where geometry errors and a degeneration of modes can be avoided. In Fig. 6, the results of the convergence study are displayed. As expected, the numerical formulation based on the complete linear space approximation (12 DoFs/cell) exhibits the same convergence behavior as its reduced functional space variant (6 DoFs/cell) but in contrary to it the former is less accurate in terms of frequency modeling.

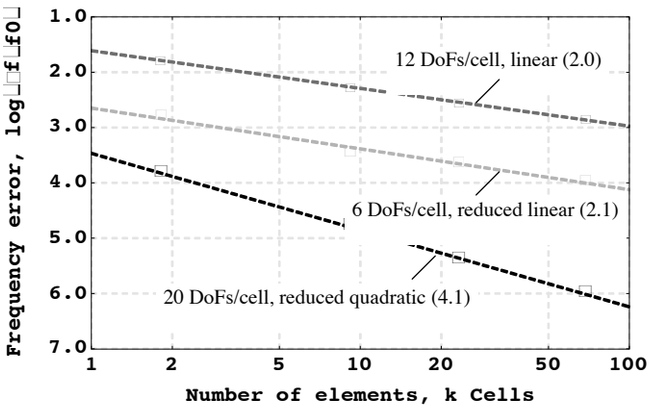


Fig. 6. Convergence analysis of various FEM approximations based on the resonance frequency of the TE/TM 110 mode in a brick shaped resonator with perfect electric conductive boundary conditions. The specified frequency error Δf is given with respect to the analytical solution $f_0$.

## VI. Application

In particle accelerators, charged particles are used for photon science and particle physics research. The actual acceleration of the particles can be effectively performed for example with the superconducting TESLA cavities which have been developed at DESY in the framework of an international collaboration [25]. Additionally to the accelerating structures which are designed to operate at a frequency of 1.3 GHz, a supplementary type of resonator working at 3.9 GHz is installed to reduce the nonlinear distortions in the longitudinal phase space of the charged particle distribution [26]. A geometrical model of the so called 3rd harmonic cavity is shown in Fig. 7, where additionally to the essential input power coupler the indispensable higher order mode (HOM) couplers are included to extract undesired modes.

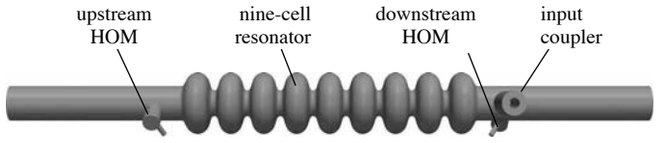


Fig. 7. Geometrical model of the TESLA 3rd harmonic cavity including the nine-cell resonator with long beam tubes as well as the input coupler and two attached higher order mode (HOM) couplers.

For detailed beam dynamics studies it is of fundamental importance to determine the field distribution within the superconducting resonators as well as the corresponding resonance frequency with a high precision. Apart from an accurate description of the cavity shape, the computational model also has to include fine geometric details representing the structure of the input and HOM couplers [26]-[28]. The challenging demand for a high precision calculation entails a proper amount of degrees of freedom which can be handled efficiently in a parallel programming environment. In Fig. 8, one of the possible decompositions of the computational domain employing the strategy described in Section IV is shown.

Fig. 8. Partitioning of the computational domain among 64 processes. A unique color is assigned to each of the sub domains. Their quantity can be adjusted according to the problem size and available computational resources.

According to the proposed field of application, the 3rd harmonic cavity is not operated with the fundamental but rather with the last of those modes composing the lowest pass band. Due to the design of the resonator with nine elementary cells connected in series, the desired mode is located inside the spectrum and efficient algorithms have to be applied to extract the desired value. One of the possible approaches is given with our parallel implementation of the Jacobi-Davidson eigenvalue solver which is capable to select modes within the spectrum without the numerically expensive procedure to repeatedly solve linear systems with high accuracy [24]. The clustered distribution of the eigenvalues allows a specification of the target frequency such that together with a proper search direction a robust extraction of the desired mode can be enabled. In Fig. 9, the location of the lowest eigenvalues is visualized and the selection process is illustrated.

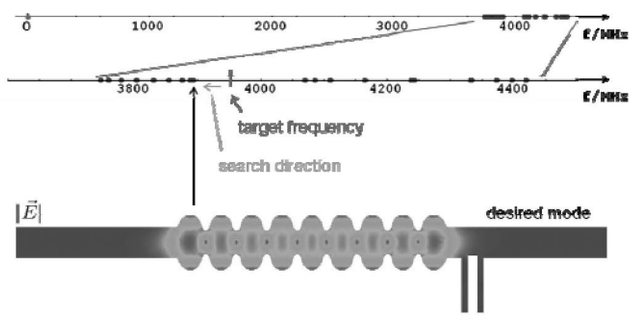


Fig. 9. Lowest part of the frequency spectrum determined for the TESLA 3rd harmonic cavity including the location of the desired eigenvalue within the distribution. Efficient calculation of the underlying eigenvalue problem can be performed with the help of the Jacobi-Davidson method in combination with a properly chosen target frequency and search direction.

On account of a large computational grid which is necessary to resolve fine geometrical details, the solution of the linear

system within the Jacobi-Davidson method turns out to become a crucial point of the algorithm even for moderate accuracy requests. Starting from a given search space $V$ which is supposed to be expanded in the direction $\Delta\vec{v}$, the system

$$P^{\mathrm{T}}(A-\lambda B)P\ \Delta\vec{v} = -P^{\mathrm{T}}\vec{r} \qquad (16)$$

with the residuum $\vec{r} = (A-\lambda B)\vec{x}$ belonging to the current approximation of the aspired eigenvector $\vec{x}$ in combination with the projector $P = I - VV^{\mathrm{T}}B$ has to be solved.

A dedicated preconditioner of the form

$$M_{\mathrm{JD}} = M^{-1} - M^{-1}V_B\left(V_B^{\mathrm{T}}M^{-1}V_B\right)^{-1}V_B{}^{\mathrm{T}}M^{-1} \qquad (17)$$

is used to enable the application of any preconditioner $M^{-1}$ to the system $A-\lambda B$ even for the projected version (16). The abbreviation $V_B = BV$ is introduced here to simplify the notation. On the basis of the geometrical model displayed in Fig. 7, together with a fine computational grid and a decomposition of the domain according to Fig. 8, the eigenvalue problem can be solved with a high precision. The iterative procedure has to be stopped if the residual error meets the required accuracy requirement. In Fig. 10, the convergence history for various discretization levels is visualized.

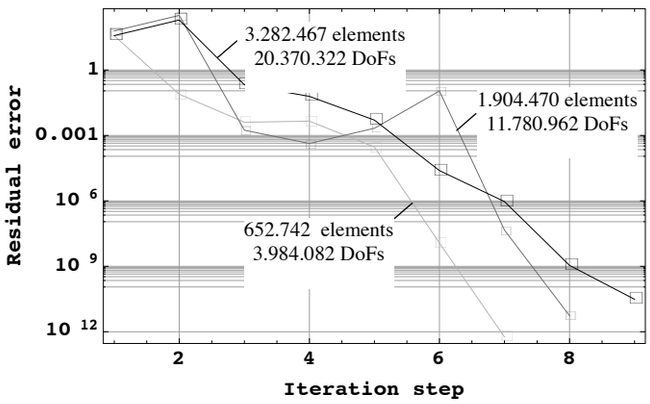


Fig. 10. Convergence history of the iterative eigenvalue solver showing accurate results for increasing number of vectors in the search space. A proper preconditioner enables the calculation of the aspired eigenvalues almost independent of the underlying problem size.

Apart from the specified eigenvalue formulation also the field representation has to cope with the high precision demands. Compared to the strongly dominating longitudinal components of the electric field strength in the vicinity of the geometrical axis, the existing transverse components arising due to the asymmetrical main input coupler as well as the higher order modes couplers are up to three orders of magnitude smaller.

Because of the general inability to model the analytical field distribution of the specified resonator precisely on the discrete level, the projection of the strong longitudinally oriented field on the set of applied basis functions results in artificial transverse field components for those elements which are located near the geometrical axis. This observation is true for all kinds of basis functions which are not able to represent the analytical field distribution but can be realized most easily for the lowest order polynomial representations. In Fig. 14 and 15, the mentioned coupling can be observed on the coarse as well as on the fine mesh resolution for various FEM approximation functions in terms of artificial noise.

This undesired behavior cannot be completely avoided but it can be reduced dramatically during the evaluation process in case the undesired transversal components cancel each other. This cancellation effect happens if local symmetric mesh cells are involved in the field evaluation process. In Fig. 11, the possible approaches are presented.

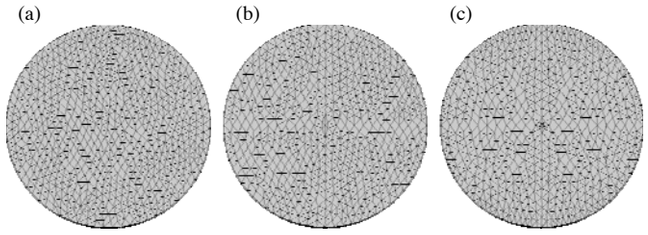


Fig. 11. Cross section of a tetrahedral mesh in a plane normal to the longitudinal axis of the resonator for an arbitrary unstructured mesh (a), a mesh aligned at the coordinate planes (b) and a true symmetric mesh (c).

A symmetric mesh at least in the region where strong longitudinal electric field components are expected can be established according to a procedure visualized in Fig. 12. An initial mesh is set up for ¼ of the model and has to be completed in a subsequent processing step.

Fig. 12. Geometrical model of the TESLA 3rd harmonic cavity used to set up a partially symmetric mesh. Initially, in the resonator region, only ¼ of the model is used for meshing. In a subsequent step, the obtained tetrahedral elements are mirrored into the missing quadrants. Special care has to be taken in the interface planes.

On the basis of a properly constructed computational mesh, the eigenvalue calculation can be initiated. An overview of the distribution of the absolute value of the electric field strength together with the appropriate absolute value of the magnetic flux density is given in Fig. 13 for the desired mode.


Fig. 13. Distribution of the absolute value of the electric field strength in (a) and the absolute value of the magnetic flux density in (b) for the operating mode. The upper part of the geometry is suppressed for visualization reasons.

A detailed analysis of the beam dynamics in the cavity region requires the precise knowledge of the electromagnetic field components preferably in the vicinity of the reference path near the cavity axis. The required components are specified according to a Cartesian coordinate system with *x* identifying the horizontal, *y* the vertical and *z* the longitudinal direction. In Fig. 14 to Fig. 17, the calculated field components $E_x$, $E_y$ and $E_z$ normalized to the maximum longitudinal value $E_{z0}$ for different approximation schemes and varying mesh resolutions are plotted.

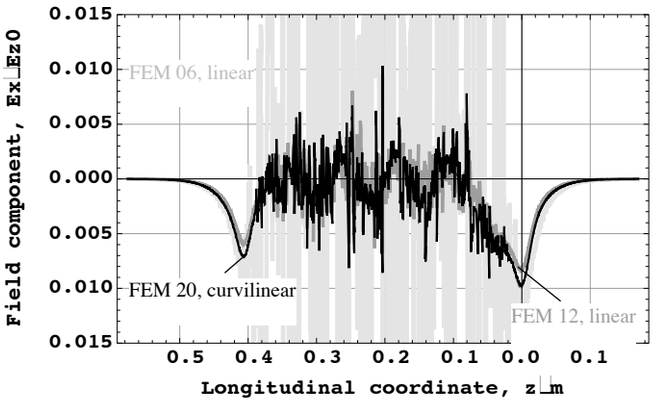


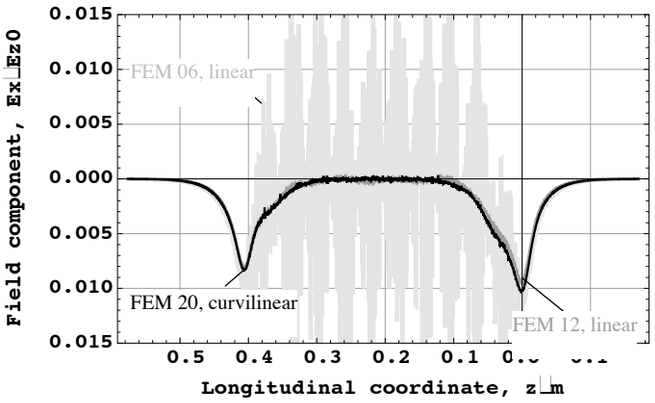


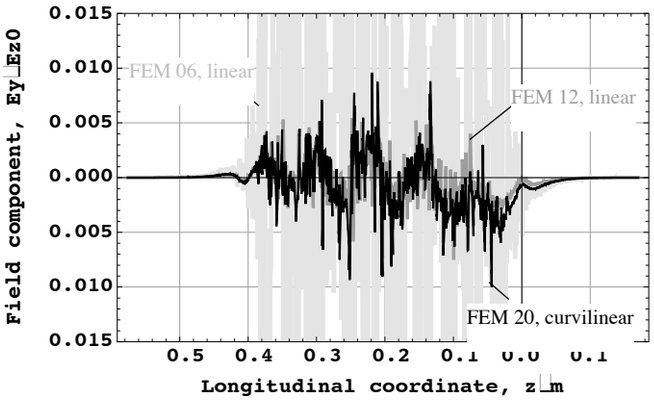


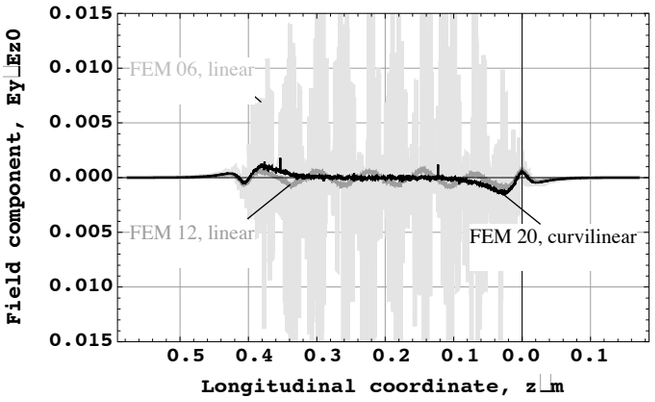


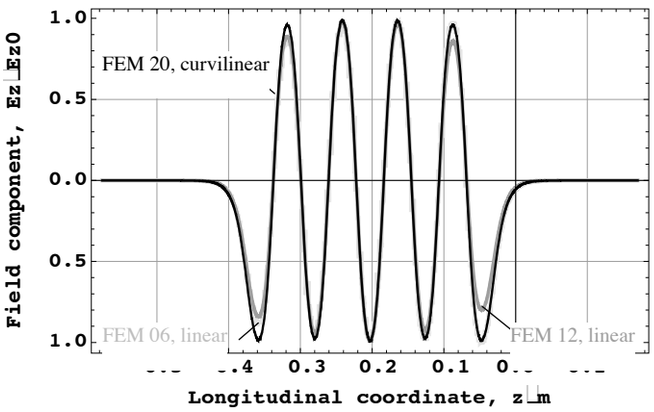


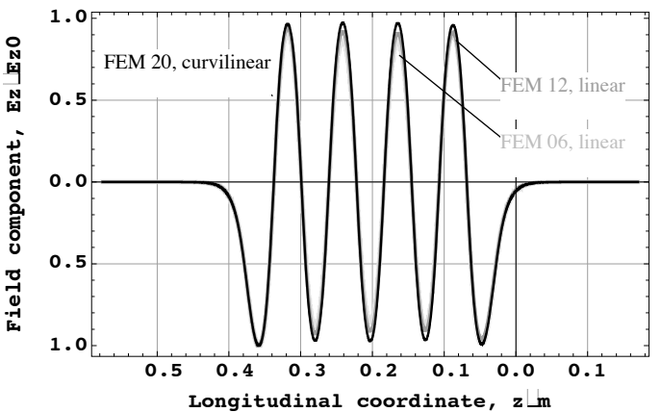


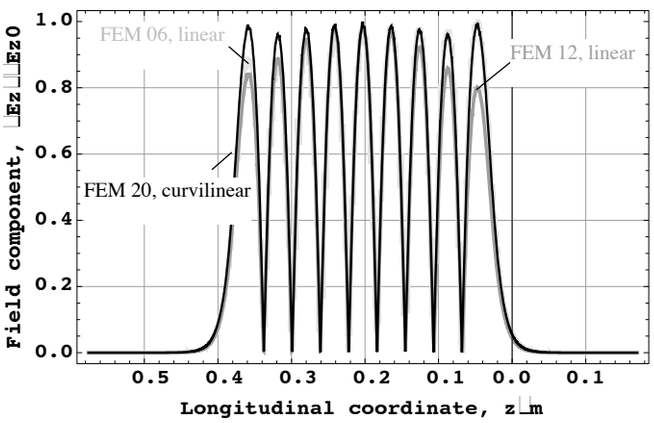


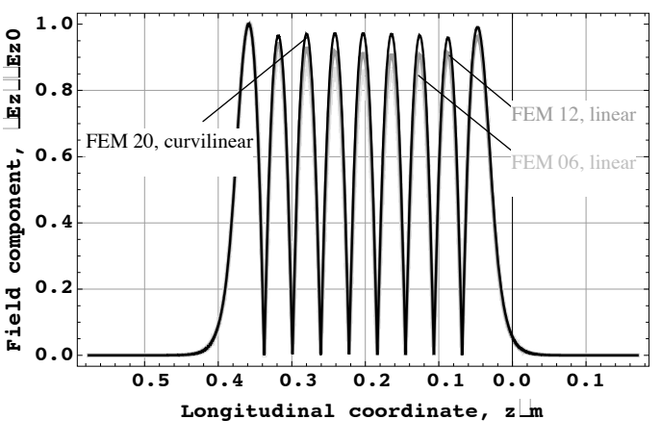


Fig. 14. Evaluation of the electric field strength along the cavity axis. All Cartesian components are normalized to the maximum longitudinal field value $E_{z0}$. The computational mesh consists of **607.576 tetrahedral elements** where no symmetry in the mesh structure is used. All calculations are performed using the reduced linear (FEM 06), the full linear (FEM 12) as well as the reduced quadratic (FEM 20) functional spaces on linear or curvilinear geometry transformation.

Fig. 15. Evaluation of the electric field strength along the cavity axis. All Cartesian components are normalized to the maximum longitudinal field value $E_{z0}$. The computational mesh consists of **2.064.944 tetrahedral elements** where no symmetry in the mesh structure is used. All calculations are performed using the reduced linear (FEM 06), the full linear (FEM 12) as well as the reduced quadratic (FEM 20) functional spaces on linear or curvilinear geometry transformation.

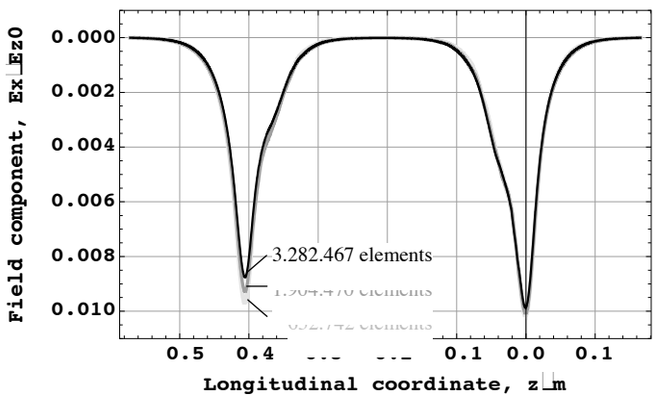


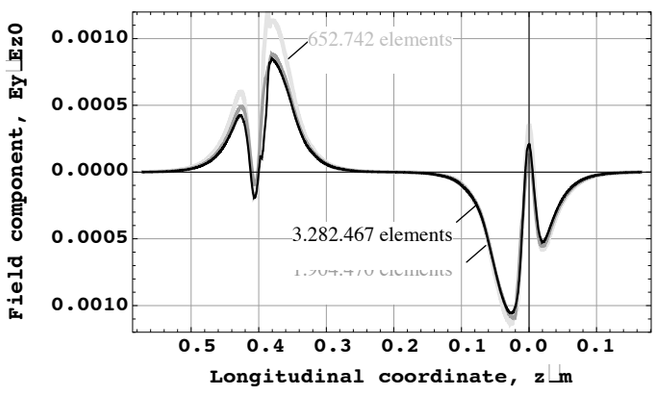


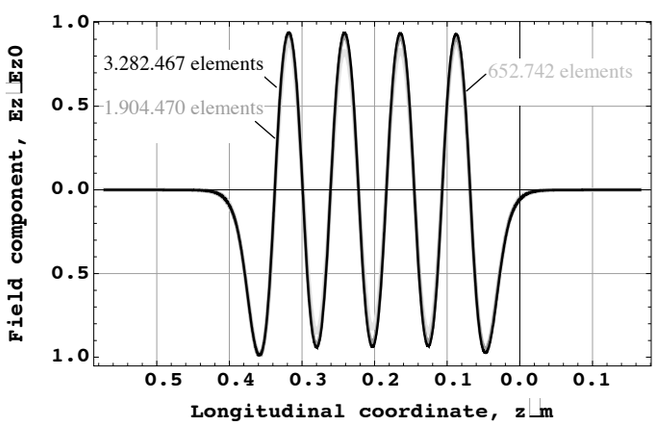


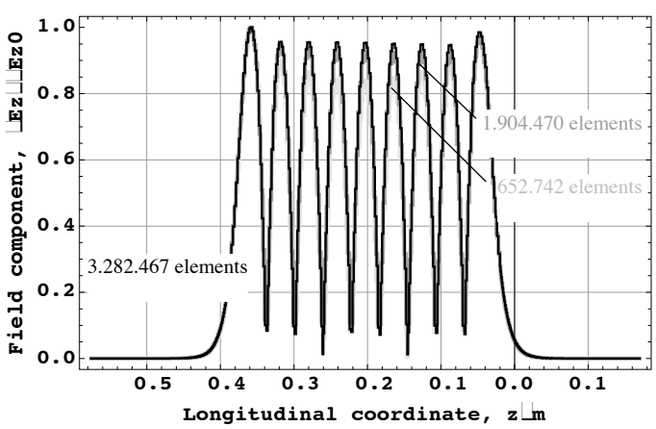


Fig. 16. Evaluation of the electric field strength along the cavity axis. All Cartesian components are normalized to the maximum longitudinal field value $E_{z0}$. The underlying functional space is given by the **reduced linear polynomial approach** (FEM 06) where a symmetric tetrahedral mesh within the cavity region is constructed automatically. A linear geometry transformation is used for the specified elements throughout the calculations.

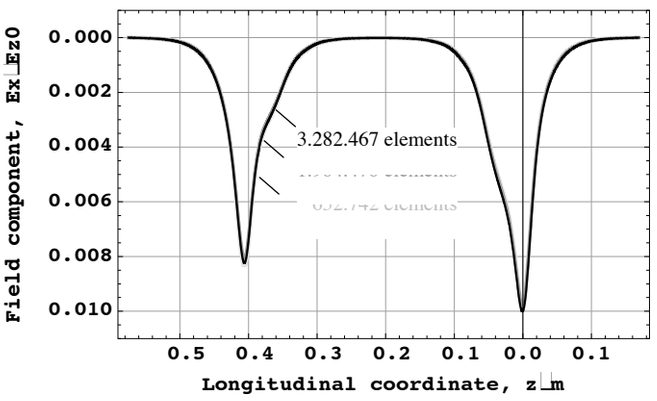


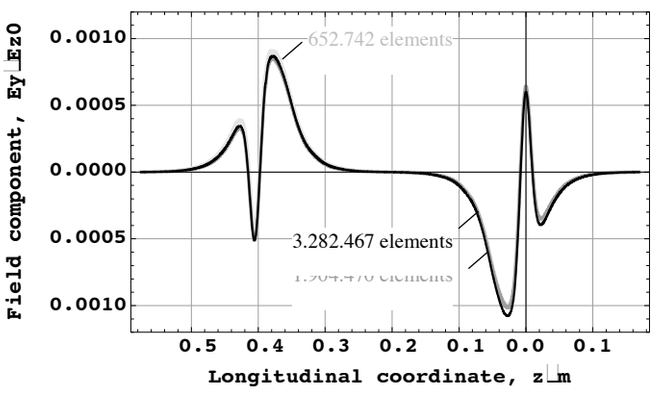


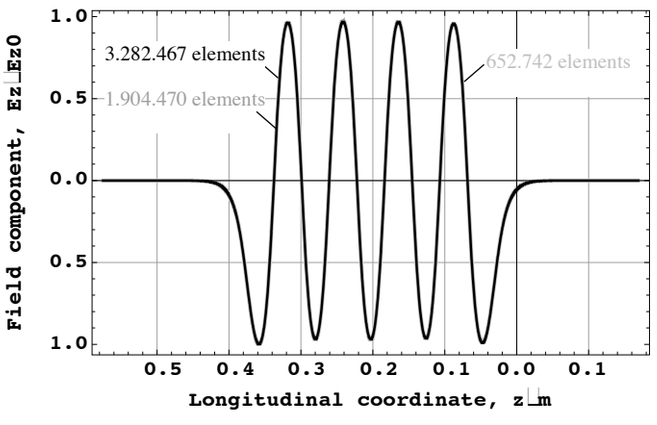


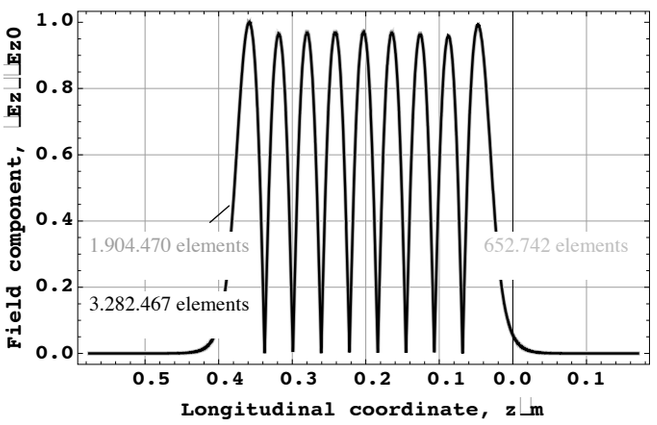


Fig. 17. Evaluation of the electric field strength along the cavity axis. All Cartesian components are normalized to the maximum longitudinal field value $E_{z0}$. The underlying functional space is given by the **reduced quadratic polynomial approach** (FEM 20) where a symmetric tetrahedral mesh within the cavity region is constructed automatically. A curvilinear geometry transformation is used for the specified elements throughout the calculations.

According to the results visualized in Fig. 14 and 15, the calculated transverse field components based on the reduced linear polynomial approximation exhibit an enormous amount of parasitic oscillation when they are evaluated on an asymmetric mesh. On the specified computational grids, the observed fluctuations are multiple times higher than the expected field quantity itself which prohibits in this stage the field data usage for beam dynamics studies. Further refinements of the mesh reduce this effect at the expense that extremely fine mesh cells have to be provided.

The situation changes dramatically if at least the complete linear function space is considered in the numerical analysis. While on a coarse mesh still a considerable amount of noisy oscillations is present, the calculations on a refined mesh show noticeable improvements. A careful inspection of the data reveals that another type of error remains which can be attributed to the mismatch of the electrical and the geometrical axis of the resonator due to the introduction of an asymmetric computational grid. Similar oscillations occur in case of a truly symmetric field which is evaluated off the axis. The worse approximation capability of the complete linear function spaces with respect to the frequency compared to the reduced variants, as gathered in Fig. 6, is indicated here by the poor representation of the longitudinal field profile |Ez| according to Fig. 14 and 15. Even though the calculated field components are much smoother, they are still unsuited for detailed beam dynamics studies.

An alternative calculation can be obtained when the known formulations are evaluated on a truly symmetric mesh. On the one hand, the high frequency oscillations are completely eliminated due to cancellation in pairs of the local field approximation errors. On the other hand, the mesh symmetry enforces the coincidence of the electrical and the mechanical axes and prevents therefore oscillations with respect to numerically misaligned cavity cells. From Fig. 16 it can be noticed that even for the reduced linear approximation approach (FEM 06), no artificial oscillations in the field distribution emerge. According to the data no convergence of the field components is yet achieved for the specified meshes. Application of the computationally more expensive reduced quadratic polynomial approach (FEM 20) on the same set of meshes consistently results in the more accurate simulation data specified in Fig. 17. Even for the sensitive horizontal electric field component $E_y$, no apparent differences can be observed.

Apart from the field components, a further important parameter within the eigenvalue calculation is the resonance frequency of the cavity for the specified mode. In Table I, a comparative study of the numerical solution process on the basis of the FEM with first (6 DoFs/cell) and second (20 DoFs/cell) order field approximation is performed for different meshes each with respect to linear and curvilinear geometry transformation. Here, the number of DoFs for each computational task is given as an indication for the underlying numerical effort. Contrary to what has been observed in case of the spherical resonator, the advantage of the curvilinear transformation cannot always be realized in this practical application. While the more accurate geometry transformation does not help to increase the accuracy under first order field approximation, a clear improvement can be observed in connection with the second order field approximation.

TABLE III. DETERMINATION OF THE RESONANCE FREQUENCY OF THE OPERATIONAL MODE OF THE TESLA 3RD HARMONIC CAVITY FOR FIRST AND SECOND ORDER FINITE ELEMENT APPROXIMATIONS USING LINEAR AND CURVILINEAR GEOMETRICAL TRANSFORMATION.

| Mesh | FEM 06, first order | | FEM 20, second order | |
|---|---|---|---|---|
| | linear | curvilinear | linear | curvilinear |
| 652.742 cells | 716.476 DoFs | | 3.984.082 DoFs | |
| | 3,8930 GHz | 3,8896 GHz | 3,9026 GHz | 3,8998 GHz |
| 1.904.470 cells | 2.137.087 DoFs | | 11.780.962 DoFs | |
| | 3,8981 GHz | 3,8961 GHz | 3,9021 GHz | 3,9001 GHz |
| 3.282.467 cells | 3.702.748 DoFs | | 20.370.322 DoFs | |
| | 3,8992 GHz | 3,8974 GHz | 3,9019 GHz | 3,9001 GHz |

In addition to the presented Cartesian components of the electric field strength, also the transverse components of the magnetic flux density are required to initiate detailed beam dynamic simulations. According to the Lorentz force equation

$$\vec{F} = q\left(\vec{E} + \vec{v} \times \vec{B}\right) \tag{18}$$

and the assumption that a particle of charge $q$ travels along the cavity axis with speed of light, the remaining components $c_0 B_x$ and $c_0 B_y$ have to be determined. Applying the curl operator on the electric field strength as specified in (1) and scaling the resulting field with the inverse of the angular frequency result in the missing components. On the basis of a quadratic field approximation, the results are displayed in Fig. 18.

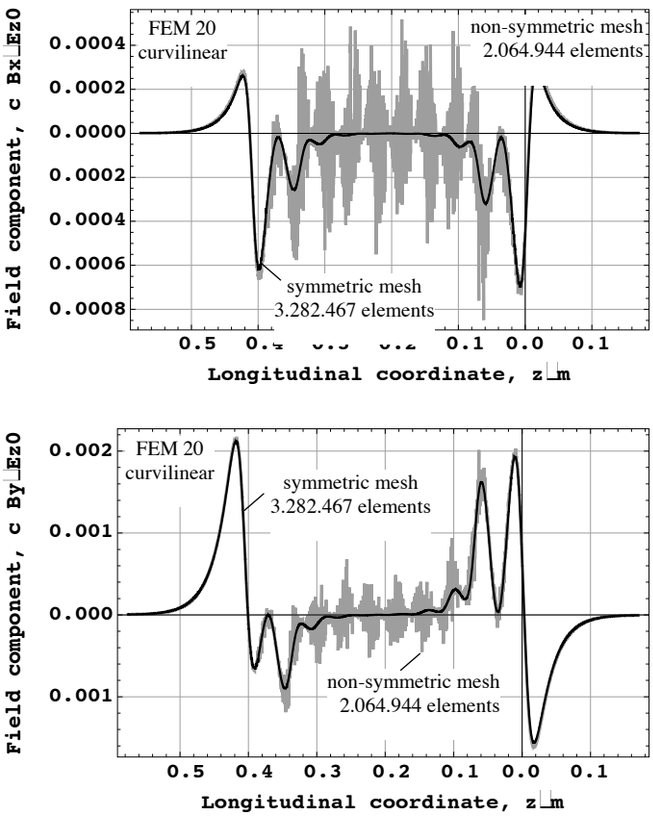


Fig. 18. Horizontal and vertical component of the magnetic flux density relative to the absolute maximum of the longitudinal electric field strength evaluated along the geometrical axis of the cavity. A reduced quadratic field approximation (FEM 20) together with a curvilinear geometry representation is used on symmetrical and unsymmetrical meshes.

## VII. Conclusion

In this article the successive application of a parallel FEM eigenvalue solver on the basis of curvilinear tetrahedral elements is reported. The superior convergence rate of higher order approximations versus lower order variants can be preserved even on non-flat material interfaces with the usage of a moderate geometrical transformation order. Parasitic high frequency oscillations in the transverse field components evaluated along the cavity axis are attributed to arbitrary tetrahedral meshes. They can be completely eliminated using a symmetric arrangement of the elements with respect to the coordinate planes in the vicinity of the evaluation region.

## VIII. Acknowledgement

The Authors thank Martin Dohlus from DESY, Germany, as well as Erion Gjonaj and Wolfgang F.O. Müller from the Technische Universitaet Darmstadt, Germany, for many valuable discussions on the physical problem formulations and their numerical solutions.

## IX. References

[1] Walsh, D., Emson, C.R.I., Riley, C.P., "Resonant Cavity Design Using the Finite Element Method", Eur. Part. Acc. Conf., Sitges, 1996

[2] Arbenz, P., Geus, R., Adam, S., „Solving Maxwell eigenvalue problems for accelerating cavities", *Phys. Rev. ST- Accelerators and Beams*, Vol. 4, 2001

[3] Ainsworth, M., Coyle, J., Ledger, P. D. , Morgan, K., "Computing Maxwell Eigenvalues by Using Higher Order Edge Elements in Three Dimensions", *IEEE Trans. on Magnetics*, 39(5): 2149-2153, 2003

[4] Silvester, P. P., Ferrari, R. L., *Finite Elements for Electrical Engineers*, Cambridge University Press, 1996

[5] Peterson, A. F., Ray, S. L., Mittra, R., *Computational Methods for Electromagnetics,* Oxford University Press and IEEE Press, 1998

[6] Davidson, D. B., *Computational Electromagnetics for RF and Microwave Engineering*, Cambridge University Press, 2005

[7] Webb, J. P., Forghani, B., "Hierarchal Scalar and Vector Tetrahedra", *IEEE Trans. on Magnetics*, 29(2): 1495-1498, 1993

[8] Graglia, R. D., Wilton, D. R., Peterson, A. F., "Higher Order Interpolatory Vector Bases for Computational Electromagnetics", *IEEE Trans. on Antennas and Propagation*, 45(3): 329-342, 1997

[9] Andersen, L. S., Volakis, J. L., „Hierarchical Tangential Vector Finite Elements for Tetrahedra", *IEEE Microwave and Guided Wave Letters*, 8(3): 127-129, 1998

[10] Davidson, D. B., "An Evaluation of Mixed-Order versus Full-Order Vector Finite Elements", *IEEE Trans. on Antennas and Propagation*, 51(9): 2430-2441, 2003

[11] Tsukerman, I., "Symbolic Algebra as a Tool for Understanding Edge Elements", *IEEE Trans. on Magnetics*, 39(3): 1111-1114, 2003

[12] Ingelström, P., "A New Set of H(curl)-Conforming Hierarchical Basis Functions for Tetrahedral Meshes", *IEEE Trans. on Microwave Theory and Techniques*, 54(1): 106-114, 2006

[13] Abdul-Rahman, R., Kasper, M., „Orthogonal Hierarchical Nédélec Elements", *IEEE Trans. on Magnetics*, 44(6): 1210-1213, 2008

[14] Wang, J. S., Ida, N., „Curvilinear and Higher Order 'Edge' Finite Elements in Electromagnetic Field Computation", *IEEE Trans. on Magnetics*, 29(2): 1491-1494, 1993

[15] Villeneuve, D., Webb, J. P., "Exact Treatment of Curved Boundaries Finite Elements by Re-Parameterization", *IEEE Trans. on Magnetics*, 36(4): 1527-1530, 2000

[16] Martini, E. , Selleri, S., "Innovative class of curvilinear tetrahedral elements", *IEE Electronics Letters*, 37(9): 557- 558, 2001

[17] Marais, N., Davidson, D. B., "Numerical Evaluation of Hierarchical Vector Finite Elements on Curvilinear Domains in 2-D", *IEEE Trans. on Antennas and Propagation*, 54(2): 734-738, 2006

[18] Swartz, J. P., Davidson, D. B., "Curvilinear Vector Finite Elements Using a Set of Hierarchical Basis Functions", *IEEE Trans. on Antennas and Propagation*, 55(2): 440-446, 2007

[19] CST AG – Computer Simulation Technology, CST Studio Suite 2009, www.cst.com

[20] Quinn, M. J., *Parallel Programming in C with MPI and OpenMP*, 1st ed., McGraw-Hill Companies, Inc., Singapore, 2003

[21] Karypis, G., Schloegel, K., Kumar, V., ParMeTiS - *Parallel Graph Partitioning and Sparse Matrix Ordering Library*, Version 3.1, University of Minnesota, 2003

[22] Balay, S., Gropp, W.D., McInnes, L.C., Smith, B.F., *PETSc Users Manual*, ANL-95/11 - Revision 3.0, Argonne National Laboratory, 2008

[23] Lee, L. Q., Li, Z., Ng, C., Ko, K., „Omega3P: A Parallel Finite-Element Eigenmode Analysis Code for Accelerator Cavities", *SLAC-PUB-13529*, 2009

[24] Sleijpen, G. L. G., Van der Vorst, H. A., A Generalized Jacobi-Davidson iteration method for linear eigenvalue problems, University Utrecht, Department of Mathematics, Preprint nr. 856, June 1994

[25] Deutsches Elektronen-Synchrotron, www.desy.de

[26] Sekutowicz, J., Wanzenberg, R., Müller, W. F. O., Weiland, T., A Design of a 3rd harmonic Cavity for the TTF2 Photoinjector, *TESLA-FEL 2002-05*, July 2002

[27] Khabibouline, T., Solyak, N., Wanzenberg, R., Higher Order Modes of a 3rd Harmonic Cavity with an Increased End-cup Iris, *TESLA-FEL 2003-01*, May 2003

[28] Gjonaj, E., Ackermann, W., Lau, T., Weiland, T., Dohlus, M., „Coupler Kicks in the Third Harmonic Module for the XFEL", *Proceedings of the 2009 Particle Acceleration Conference*, 2009

## X. Authors name and affiliation

Wolfgang Ackermann, Technische Universitaet Darmstadt, Institut fuer Theorie Elektromagnetischer Felder (TEMF), Schlossgartenstrasse 8, D 64289 Darmstadt, Germany, Tel.: +49 6151-162261, e-mail: ackermann@temf.tu-darmstadt.de

Galina Benderskaya, CST AG – Computer Simulation Technology, Bad Nauheimer Strasse 19, D 64289 Darmstadt, Germany, Tel.: +49 6151-73030, e-mail: galina.benderskaya @cst.com

Thomas Weiland, Technische Universitaet Darmstadt, Institut fuer Theorie Elektromagnetischer Felder (TEMF), Schloss-gartenstrasse 8, D 64289 Darmstadt, Germany, Tel.: +49 6151-162161, e-mail: thomas.weiland@temf.tu-darmstadt.de